

# A new analytic approach to infer the cosmic-ray ionization rate in hot molecular cores from HCO<sup>+</sup>, N<sub>2</sub>H<sup>+</sup>, and CO observations

Gan Luo<sup>1</sup>, Thomas G. Bisbas<sup>2</sup>, Marco Padovani<sup>3</sup>, and Brandt A. L. Gaches<sup>4</sup>

<sup>1</sup> Institut de Radioastronomie Millimetrique, 300 rue de la Piscine, 38400, Saint-Martin d'Hères, France  
e-mail: luo@iram.fr

<sup>2</sup> Research Center for Astronomical Computing, Zhejiang Laboratory, Hangzhou 311100, China  
e-mail: tbi@zhejianglab.com

<sup>3</sup> INAF-Osservatorio Astrofisico di Arcetri, Largo E. Fermi 5, 50125 Firenze, Italy

<sup>4</sup> Department of Space, Earth and Environment, Chalmers University of Technology, Gothenburg SE-412 96, Sweden

Received xx; accepted xx

## ABSTRACT

**Context.** The cosmic-ray ionization rate ( $\zeta_2$ ) is one of the key parameters in star formation, since it regulates the chemical and dynamical evolution of molecular clouds by ionizing molecules and determining the coupling between the magnetic field and gas.

**Aims.** However, measurements of  $\zeta_2$  in dense clouds (e.g.,  $n_{\text{H}} \geq 10^4 \text{ cm}^{-3}$ ) are difficult and sensitive to the model assumptions. The aim is to find a convenient analytic approach that can be used in high-mass star-forming regions (HMSFRs), especially for warm gas environments such as hot molecular cores (HMCs).

**Methods.** We propose a new analytic approach to calculate  $\zeta_2$  through HCO<sup>+</sup>, N<sub>2</sub>H<sup>+</sup>, and CO measurements. By comparing our method with various astrochemical models and with observations found in the literature, we identify the parameter space for which the analytic approach is applicable.

**Results.** Our method gives a good approximation, to within 50%, of  $\zeta_2$  in dense and warm gas (e.g.,  $n_{\text{H}} \geq 10^4 \text{ cm}^{-3}$ ,  $T = 50, 100 \text{ K}$ ) for  $A_{\text{V}} \geq 4 \text{ mag}$  and  $t \geq 2 \times 10^4 \text{ yr}$  at Solar metallicity. The analytic approach gives better results for higher densities. However, it starts to underestimate the CRIR at low metallicity ( $Z = 0.1Z_{\odot}$ ) and high CRIR ( $\zeta_2 \geq 3 \times 10^{-15} \text{ s}^{-1}$ ). By applying our method to the OMC-2 FIR4 envelope and the L1157-B1 shock region, we find  $\zeta_2$  values of  $(1.0 \pm 0.3) \times 10^{-14} \text{ s}^{-1}$  and  $(2.2 \pm 0.4) \times 10^{-16} \text{ s}^{-1}$ , consistent with those previously reported.

**Conclusions.** We calculate  $\zeta_2$  toward a total of 82 samples in HMSFRs, finding that the average value of  $\zeta_2$  toward all HMC samples ( $\zeta_2 = (7.4 \pm 5.0) \times 10^{-16} \text{ s}^{-1}$ ) is more than an order of magnitude higher than the theoretical prediction of cosmic-ray attenuation models, favoring the scenario that locally accelerated cosmic rays in embedded protostars should be responsible for the observed high  $\zeta_2$ .

**Key words.** Stars: formation – ISM: cosmic rays – ISM: abundances – ISM: molecules – ISM: clouds – astrochemistry

## 1. Introduction

Cosmic rays (CRs) play a major role in the physical and chemical evolution of dense clouds. In well-shielded regions where far-ultraviolet (FUV) photons cannot penetrate, namely where the visual extinction ( $A_{\text{V}}$ ) is larger than 3–4 mag (Wolfire et al. 2010), CRs initiate the chemistry by ionizing various molecules and producing ions (e.g., H<sub>3</sub><sup>+</sup>)<sup>1</sup>. On the other hand, CRs determine the degree of ionization in dense clouds and regulate the coupling between the magnetic field and gas, which, in turn, affects the dynamic timescale during the star formation process (Dalgarno 2006; Padovani et al. 2014, 2020; Padovani & Gaches 2024).

Ions (e.g., H<sub>3</sub><sup>+</sup>, OH<sup>+</sup> and H<sub>2</sub>O<sup>+</sup>) are the most favored tracers to constrain the cosmic-ray ionization rate (CRIR), since the formation and destruction of these species are relatively simple and allow us to estimate almost directly the CRIR (Gerin et al. 2010; Indriolo & McCall 2012; Indriolo et al. 2015; Neufeld & Wolfire 2017). In dense clouds, such methodology is, however, not available due to the large extinction and low abundance of the above-mentioned ions.

<sup>1</sup> Assuming no other sources of ionization (e.g., X-rays in the vicinity of supernova remnants, Yusef-Zadeh et al. 2003; Indriolo 2023).

The abundance ratios of DCO<sup>+</sup>/HCO<sup>+</sup> and HCO<sup>+</sup>/CO have been proposed to infer the ionization fraction and CRIR in cold prestellar cores (Caselli et al. 1998). However, the deuteration ratios are sensitive to the initial ortho-to-para ratio, the evolution timescale, and the source physical conditions (e.g., gas density and temperature, Shingledecker et al. 2016). Thus, the resultant CRIR from the above method could be overestimated by several orders of magnitude (Sabatini et al. 2023; Redaelli et al. 2024). More recently, an analytic approach using ortho-H<sub>2</sub>D<sup>+</sup> and CO was proposed to estimate the CRIR (Bovino et al. 2020) in cold prestellar cores where depletion of molecules is crucial. In addition, rovibrational H<sub>2</sub> lines could be a potentially useful method to derive CRIR value in the cold molecular cloud (Bialy 2020; Padovani et al. 2022; Bialy et al. 2022; Gaches et al. 2022a), which would be, in principle, detected by the James Webb Space Telescope (JWST).

In high-mass star-forming regions (HMSFRs), the gas temperature increases in the more evolved phase (e.g.,  $T \sim 100 \text{ K}$  in hot molecular cores, HMCs, Blake et al. 1987; Beuther et al. 2007b; Luo et al. 2019; Qin et al. 2022), depletion and deuteration are inefficient, so that the methods described above cannot be adopted. Over the past decade, different molecular line tracers combined with astrochemical models have been used to

probe the CRIR in HMSFRs, such as  $\text{HCO}^+$  and  $\text{N}_2\text{H}^+$  (Cecarelli et al. 2014b; Redaelli et al. 2021), and carbon-chain molecules (e.g.,  $\text{HC}_3\text{N}$ ,  $\text{HC}_5\text{N}$ , Fontani et al. 2017; Favre et al. 2018). While chemical modeling requires large computational resources, a convenient analytic approach would be useful in determining the variance of CRIR with the spatial distribution and evolution stage in HMSFRs.

In this work, we propose a new analytic approach to estimate the CRIR in HMSFRs, especially for high-mass protostellar objects (HMPOs) and HMCs. HMPOs are in a more evolved phase than the cold infrared dark cloud (IRDC). They consist of massive accreting protostars (e.g.,  $M > 8M_\odot$ ) and exhibit bright mid-infrared emission and strong outflows (Beuther et al. 2002b, 2007a; Zinnecker & Yorke 2007; Motte et al. 2018). The characteristic size of HMPOs is  $\sim 0.5$  pc, and the average density is between  $10^4$  and  $10^6 \text{ cm}^{-3}$  (Beuther et al. 2002a). HMCs appear in the later stage of HMPOs and are characterized by high gas temperatures (e.g.,  $T \gtrsim 100$  K), densities ( $n_{\text{H}} \gtrsim 10^6 \text{ cm}^{-3}$ ), and rich molecular lines (Blake et al. 1987; Kurtz et al. 2000; Beuther et al. 2007b; Qin et al. 2022). We compare our approach with chemical simulations from 3D-PDR and UCLCHEM and demonstrate that our method can give a good estimation of CRIR for HMPOs and HMCs.

The paper is organized as follows. We present the chemical analysis and describe the analytic approach in Sect. 2. In Sect. 3, we compare our approach with chemical simulations. We apply our method to two well-known sources and compare our results with previous modeling in the literature in Sect. 4. The uncertainties and robustness of the approach are also discussed. In Sect. 5, we calculate the CRIR toward a large sample of HMSFRs. The main results and conclusions are summarised in Sect. 6.

## 2. Methods

### 2.1. Chemical analysis

We describe, below, the formation and destruction reactions of  $\text{H}_3^+$ ,  $\text{HCO}^+$ ,  $\text{N}_2\text{H}^+$ , and  $\text{H}_3\text{O}^+$  in dense and warm clouds (e.g.,  $n_{\text{H}} \geq 10^4 \text{ cm}^{-3}$ ,  $T \geq 50$  K), where the depletion is negligible.

The formation of  $\text{H}_3^+$  in dense clouds starts from the ionization of  $\text{H}_2$  by CRs (see, e.g., Glassgold & Langer 1973):



Then,  $\text{H}_3^+$  can be removed by the most abundant neutral species (Indriolo & McCall 2012):



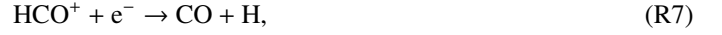
and electrons:



Reactions R3 and R4 are the main formation channels of  $\text{HCO}^+$ <sup>2</sup> and  $\text{N}_2\text{H}^+$ , respectively.

<sup>2</sup> Reaction R8 below also contribute to the formation of  $\text{HCO}^+$  but with a minor role.

The corresponding destruction channels of  $\text{HCO}^+$  and  $\text{N}_2\text{H}^+$  are (Dalgarno 2006):



and<sup>3</sup>



Considering reactions R1-R6, CRIR ( $\zeta_2$ , referring to the ionization rate of  $\text{H}_2$ ) can be written as:

$$\zeta_2 = \frac{n(\text{H}_3^+)}{n(\text{H}_2)} [n(\text{CO})k_{\text{R3}} + n(\text{N}_2)k_{\text{R4}} + n(\text{O})k_{\text{R5}} + n(\text{e}^-)k_{\text{R6}}]. \quad (1)$$

Similarly, from reactions R4 and R8–R10 we can write:

$$n(\text{H}_3^+)n(\text{N}_2)k_{\text{R4}} = n(\text{N}_2\text{H}^+) [n(\text{CO})k_{\text{R8}} + n(\text{e}^-)k_{\text{R9}} + n(\text{O})k_{\text{R10}}]. \quad (2)$$

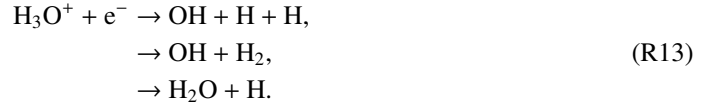
Considering the charge balance, the number density of electrons should be equal to the most abundant ions (see Appendix A):

$$n(\text{e}^-) = n(\text{HCO}^+) + n(\text{N}_2\text{H}^+) + n(\text{H}_3^+) + n(\text{H}_3\text{O}^+). \quad (3)$$

In dense clouds, the formation of  $\text{H}_3\text{O}^+$  starts from reaction R5. Then, it hydrogenates to form  $\text{H}_2\text{O}^+$  and  $\text{H}_3\text{O}^+$  (Bialy & Sternberg 2015; Indriolo et al. 2015; Luo et al. 2023b):



Electron recombination reactions dominate the destruction of  $\text{H}_3\text{O}^+$ :



From reactions R5, R10, and R11-R13,  $n(\text{H}_3\text{O}^+)$  can be written as:

$$n(\text{H}_3\text{O}^+) = \frac{n(\text{O})n(\text{H}_3^+)k_{\text{R5}} + n(\text{N}_2\text{H}^+)n(\text{O})k_{\text{R10}}}{n(\text{e}^-)k_{\text{R13}}}. \quad (4)$$

Combining Eqs. (3) and (4),  $n(\text{H}_3^+)$  can be written as:

$$n(\text{H}_3^+) = \frac{n(\text{e}^-)^2 - n(\text{e}^-) [n(\text{HCO}^+) + n(\text{N}_2\text{H}^+)] - \alpha}{n(\text{e}^-) + n(\text{O})k_{\text{R5}}/k_{\text{R13}}}, \quad (5)$$

where  $\alpha$  is

$$\alpha = \frac{n(\text{N}_2\text{H}^+)n(\text{O})k_{\text{R10}}}{k_{\text{R13}}}, \quad (6)$$

Then,  $n(\text{e}^-)$  can be calculated from Eqs. (2) and (5):

$$n(\text{e}^-) = \frac{\beta + \sqrt{\beta^2 + 4\gamma\theta}}{2\gamma}, \quad (7)$$

<sup>3</sup> The reaction R10 is endothermic by 0.3 eV, thus, it could only occur under specific conditions (e.g., shocked or turbulent environments). Considering the small reaction rate of R10 (Table B.1), ignoring it would only contribute a marginal decrease ( $\sim 10\%$ ) to the calculated  $\zeta_2$  using the analytic approach.

where

$$\beta = \frac{n(\text{N}_2\text{H}^+)}{n(\text{N}_2)k_{\text{R}4}} \left[ \frac{n(\text{O})k_{\text{R}5}k_{\text{R}9}}{k_{\text{R}13}} + n(\text{CO})k_{\text{R}8} + n(\text{O})k_{\text{R}10} \right] + n(\text{HCO}^+) + n(\text{N}_2\text{H}^+), \quad (8)$$

$$\gamma = 1 - \frac{n(\text{N}_2\text{H}^+)k_{\text{R}9}}{n(\text{N}_2)k_{\text{R}4}}, \quad (9)$$

and

$$\theta = \alpha \left[ 1 + k_{\text{R}5} \frac{n(\text{CO})k_{\text{R}8} + n(\text{O})k_{\text{R}10}}{n(\text{N}_2)k_{\text{R}4}k_{\text{R}10}} \right]. \quad (10)$$

### 2.1.1. The new analytic approach

To determine  $\zeta_2$  through our new methodology it is needed:

1. a proper constraint on  $n(\text{H}_2)$ ;
2. to determine the abundances of  $\text{HCO}^+$ ,  $\text{N}_2\text{H}^+$  and CO from observations;
3. an assumption of the initial abundances of  $\text{N}_2$  and O.

In dense cores where hydrogen is mostly in molecular form, we can divide all number density terms ( $n(x)$ ) by  $n(\text{H}_2)$  in Eqs. (1) to (7). Thus, the calculated CRIR ( $\tilde{\zeta}_2$ , we distinguish between the calculated CRIR ( $\tilde{\zeta}_2$ ) and the input one ( $\zeta_2$ ) from chemical simulations) can be written as:

$$\tilde{\zeta}_2 = n(\text{H}_2)f(\text{H}_3^+) [f(\text{CO})k_{\text{R}3} + f(\text{N}_2)k_{\text{R}4} + f(\text{O})k_{\text{R}5} + f(\text{e}^-)k_{\text{R}6}], \quad (11)$$

where  $f(x)$  is the relative abundance of species “x” with respect to  $\text{H}_2$ ,  $n(\text{H}_2)$  is the number density of  $\text{H}_2$ , and  $f(\text{e}^-)$  can be obtained from Eq. 7.

For the calculations of  $\tilde{\zeta}_2$ , we use the latest reaction rates from the UMIST database (hereafter, UMIST2022, Millar et al. 2024) unless otherwise stated.

## 2.2. Chemical models

To explore the behavior of our analytic approach, we employ the publicly available astrochemical codes<sup>4</sup> 3D-PDR (Bisbas et al. 2012) and UCLCHEM (Holdship et al. 2017). 3D-PDR is a photodissociation region code that models one- and three-dimensional density distributions. It calculates the attenuation of the FUV radiation field in every depth point and outputs the self-consistent solutions of chemical abundances, gas and dust temperature, emissivities, and level populations by performing iterations over thermal balance. In the 3D-PDR models, we consider more than 200 species with 3000 reactions taken from the UMIST2012<sup>5</sup> (McElroy et al. 2013). The initial gas phase abundances of different elements are listed in Table 1. We note that the initial element abundances are not expected to be the same everywhere. However, as long as the abundances of key species do not change significantly, the assumptions and conclusions in Sect. 2.1 remain valid (see §4.1.1 for more discussion on different metallicities.). We also consider the treatment of CR attenuation incorporated into 3D-PDR, as presented in Gaches et al. (2019, 2022b). Unless

<sup>4</sup> <https://uclchem.github.io/>

<sup>5</sup> We note that the reaction rates of R5, R8, R11, and R12 have changed by up to a factor of  $\sim 3$  between the UMIST2012 and UMIST2022. In that case, we calculate  $\tilde{\zeta}_2$  in Sect. 3.1 using the reaction rates from UMIST2012 only when comparing with 3D-PDR simulations.

otherwise stated, all 3D-PDR models presented here are calculated until the thermal balance is reached.

We perform additional simulations with UCLCHEM (Holdship et al. 2017) to test how the gas-grain reactions and depletion processes influence the results. UCLCHEM is a time-dependent astrochemical code focusing on gas-grain reactions. It considers freeze-out processes, thermal, and non-thermal desorption processes and outputs the chemical abundances at a given temperature, density, and  $A_V$ . Contrary to 3D-PDR calculations where the code terminates as long as the thermal balance is reached, the simulations in UCLCHEM are isothermal. We set three temperatures in these simulations,  $T_k = 15$  K, 50 K, and 100 K. 15 K is the typical temperature of the cold dark cloud and it is below the temperature for CO desorption ( $T \sim 20$  K) (Öberg et al. 2011). 50 K is above the sublimation temperature of simple molecules (e.g., CO) but below the desorption temperature of water ice and COMs. 100 K is the typical temperature of HMCs and most of the species would be released from the ice phase (van Dishoeck 2014).

In UCLCHEM simulations, the deuterium chemical network of Majumdar et al. (2017) is adopted. To reduce the computational expense, species with molecular weight higher than 66 were excluded (mostly carbon-chain molecules and complex organic molecules that contain more than 5 carbon atoms). Excluding these molecules may not greatly impact the results since they gradually build up the abundances from C and  $\text{C}^+$ , and have little chemical connection with the simple species we mentioned above. Besides, their abundances are usually too low (e.g.,  $10^{-10}$  and below, Herbst & van Dishoeck 2009) to impact the simple species. The chemical network contains a total of  $\sim 800$  species and  $\sim 3 \times 10^4$  reactions. The initial gas-phase abundance of HD is adopted as the value measured in the Local Bubble ( $1.6 \times 10^{-5}$ , Linsky et al. 2006)<sup>6</sup>. The remaining element abundances are the same as in Table 1. For all the simulations in both 3D-PDR and UCLCHEM, the cloud radius is set as 1 pc.

## 3. Results

### 3.1. Comparison to 3D-PDR simulations

We test three uniform density clouds ( $n_{\text{H}} = 10^4$ ,  $10^5$ , and  $10^6 \text{ cm}^{-3}$ ) with different uniform CRIR ( $10^{-19} \leq \zeta_2/\text{s}^{-1} \leq 10^{-14}$ ) input. Figure 1 shows the ratio between CRIR derived from Eq. 11 and the input value ( $\tilde{\zeta}_2/\zeta_2$ ) at  $A_V = 20$  mag. In most of the simulations, the calculated CRIR from the analytic approach is within 50% of the model input. The analytic approach underestimates the input CRIR by up to a factor of 3 at  $n_{\text{H}} = 10^4 \text{ cm}^{-3}$  and  $\zeta_2 = 10^{-14} \text{ s}^{-1}$ . This is due to the destruction of CO molecules under high CRIR (Bialy & Sternberg 2015; Bisbas et al. 2015, 2017), thus, the destruction pathways we analyzed in Sect. 2.1 change. As the density increases, the analytic approach gives a more accurate result.

Figure 2 shows the deviation maps between the analytic approach and the input values at different  $A_V$  and  $\zeta_2$ . Our analytic approach gives a good approximation, to within 50%, if  $\zeta_2 \leq 5 \times 10^{-15} \text{ s}^{-1}$  and  $A_V \geq 4$  mag at  $n_{\text{H}} = 10^4 \text{ cm}^{-3}$ , and  $A_V \geq 4$  mag for any  $\zeta_2$  at  $n_{\text{H}} = 10^5 \text{ cm}^{-3}$  and  $n_{\text{H}} = 10^6 \text{ cm}^{-3}$ .

In addition, we test the CR attenuation model with a variable density distribution, in which the CR spectrum is adopted as the

<sup>6</sup> The measured D/H ratios in high column density regions are lower, presumably due to the depletion of D on dust grain (Linsky et al. 2006; Friedman et al. 2023). However, the D/H ratio only matters in our analysis for the dark cloud where depletion of molecules is significant (See Sect. 3.2).

**Table 1.** Initial gas-phase element abundances used in our simulations.

Elements	Abundance relative to H	References
H	$5 \times 10^{-1}$	/
H <sub>2</sub>	$2.5 \times 10^{-1}$	/
He	$9 \times 10^{-2}$	a
C <sup>+</sup>	$1.5 \times 10^{-4}$	b,c
O	$3 \times 10^{-4}$	d,e
N	$7.6 \times 10^{-5}$	f
S <sup>+</sup>	$8 \times 10^{-8}$	c, g
Si <sup>+</sup>	$8 \times 10^{-9}$	c, g
Mg <sup>+</sup>	$7 \times 10^{-9}$	c, g
Fe <sup>+</sup>	$3 \times 10^{-9}$	c, g
Na <sup>+</sup>	$2 \times 10^{-9}$	c, g
P <sup>+</sup>	$2 \times 10^{-10}$	c, g
Cl <sup>+</sup>	$1 \times 10^{-9}$	c, g
F <sup>+</sup>	$6.68 \times 10^{-9}$	h

**Notes.** References: (a) Wakelam & Herbst (2008). (b) Sofia et al. (1997). (c) Hincelin et al. (2011). (d) Meyer et al. (1998). (e) Lis et al. (2023). (f) Meyer et al. (1997). (g) Majumdar et al. (2017). (h) Neufeld et al. (2005).

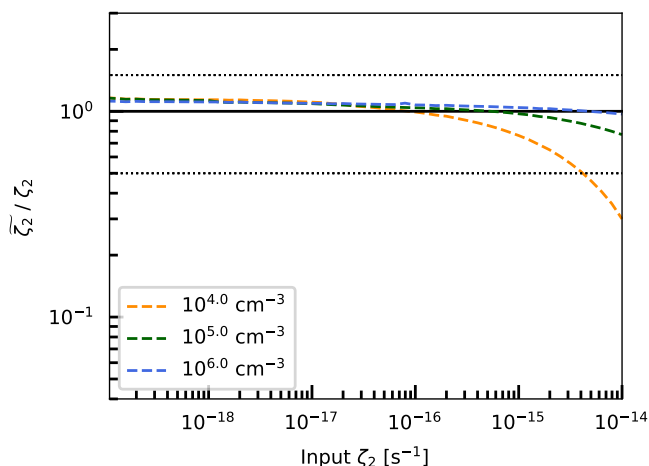


**Fig. 1.** The comparison between our approach and 3D-PDR simulations. The x-axis denotes the input CRIR of each simulation, where the CRIR in each simulation is treated as uniform. The y-axis denotes the ratio between the calculated CRIR and the input one ( $\tilde{\zeta}_2/\zeta_2$ ) at  $A_V = 20$  mag. The black horizontal line represents the fiducial value, and the horizontal dotted lines represent 50% of the deviation from the input values. Orange, green, and blue dashed lines represent results at  $n_H = 10^4$ ,  $10^5$ , and  $10^6$   $\text{cm}^{-3}$ . The external FUV intensity for all simulations is normalized to the Draine unit ( $\chi/\chi_0 = 1$ ).

high-energy spectrum model  $\mathcal{H}$  from Ivlev et al. (2015), and the density distribution of the cloud adopts the  $A_V$ - $n_H$  relation of Bisbas et al. (2023). This relation has been found to reproduce reasonably well and at a minimal computational cost, the results from computationally expensive three-dimensional astrochemical models. Figure 3 shows the comparison between the input  $\zeta_2$  and the analytical approach. At lower column densities ( $N_{\text{H}_2} < 3.4 \times 10^{21} \text{ cm}^{-2}$ , corresponding to  $n_H < 3 \times 10^3 \text{ cm}^{-3}$ ), our approach underestimates  $\zeta_2$  by over 50%. At higher column densities, our approach gives a good approximation.

### 3.2. Comparison to UCLCHEM simulations

Figure 4 shows the comparison between the analytic approach with UCLCHEM simulations for different temperatures and densities. At low temperatures ( $T_k = 15$  K), most of the species (including CO and O) would freeze out onto dust grain, the analytic approach underestimates the CRIR by a factor from a few ( $n_H = 10^4 \text{ cm}^{-3}$ ) to several orders of magnitude (at  $n_H = 10^5$  and  $10^6 \text{ cm}^{-3}$ ). This is expected since the depletion processes greatly reduce the abundances of CO, O, and  $\text{N}_2$  by several orders of magnitude such that the destruction pathways of  $\text{H}_3^+$  we considered in Sect. 2 (reactions R3-R5) are no longer the dominant  $\text{H}_3^+$  destruction mechanism. Instead, deuteration fractionation cannot be ignored such that the destruction of  $\text{H}_3^+$  and the reaction channels should involve deuterated species (Millar et al. 1989; Ceccarelli et al. 2014a; Caselli et al. 2019).

When the gas temperature is higher than the sublimation temperature of CO (the cases of  $T_k = 50$  and  $100$  K), the analytic approach gives a better estimation, to within 50% for most cases. The higher the gas temperature, the better estimation is given by the analytic approach. Our analytic approach gives a more accurate estimation for higher density simulations, the same as we found with the 3D-PDR simulations.

Figure 5 shows the deviation map between the analytic approach and the input values at different evolution timescales and  $\zeta_2$ . For early timescales, where the molecules are still building their abundances (e.g., at  $n_H = 10^4 \text{ cm}^{-3}$  and  $t \leq 10^4$  yr), the analytic approach underestimates the CRIR. At  $n_H = 10^4 \text{ cm}^{-3}$  and  $t \geq 2 \times 10^4$  yr, the analytic approach gives a reasonable  $\zeta_2$  estimation except for  $t \approx 10^5$  yr and  $\zeta_2 \approx 5 \times 10^{-16} \text{ s}^{-1}$ , where the calculated value is overestimated by a factor of 3.7. For  $n_H = 10^5 \text{ cm}^{-3}$ , the analytic approach gives a good approximation of the CRIR for the majority of the parameter space if  $t > 10^4$  yr. The maximum deviation between the analytic approach and the input value ( $\tilde{\zeta}_2/\zeta_2 = 2.6$ ) appears at  $t \approx 10^4$  yr and  $\zeta_2 \approx 5 \times 10^{-15} \text{ s}^{-1}$ . At  $n_H = 10^6 \text{ cm}^{-3}$ , the analytic approach gives a good estimate for all the parameter space we modeled. The results suggest that the analytic approach can be used for conditions of warm dense gas, namely in HMPOs and HMCs.

## 4. Discussion

### 4.1. Robustness of the analytic approach

In the above simulations, we ignore the variation of initial element abundances (e.g., in different metallicity environments), the size of the source, and the gas density and temperature during the evolution processes. In the following sections, we discuss the robustness of the analytic approach under different cases.

#### 4.1.1. Variation of metallicity

The variation of metallicity would change the initial abundances of heavy elements (heavier than He). We test three metallicities ( $Z = 0.1, 0.3$ , and  $2 Z_\odot$ , which correspond to low-metallicity, outer Galaxy/Large Magellanic Cloud (LMC), and the Galactic Center) with UCLCHEM at  $n_H = 10^6 \text{ cm}^{-3}$ . The results are shown in Fig. 6. The analytic approach gives a good estimation of  $\zeta_2$  at  $Z = 0.3$  and  $2 Z_\odot$ . However, the analytic approach starts to underestimate the value of  $\zeta_2$  at  $Z = 0.1 Z_\odot$  when the CRIR is high ( $\zeta_2 \geq 3 \times 10^{-15} \text{ s}^{-1}$ ). At  $Z = 0.1 Z_\odot$ , the abundances of heavy elements are reduced by a factor of 10, while the abundances of D and He remain the same. Furthermore, due to the high CRIR, key species like CO would be easily destroyed, leading to com-

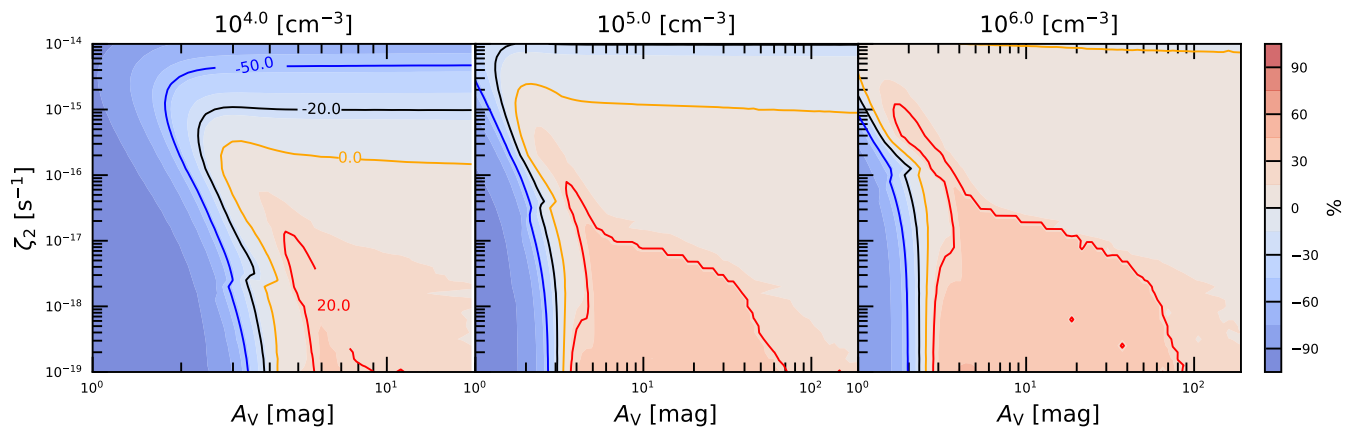


**Fig. 2.** The deviation maps between the analytic approaches and the input values at different  $A_V$  and  $\zeta_2$  for  $n_H = 10^4$  (left),  $10^5$  (middle), and  $10^6 \text{ cm}^{-3}$  (right). Red, orange, black, and blue curves denote the 20%, 0%, -20%, and -50% deviations.

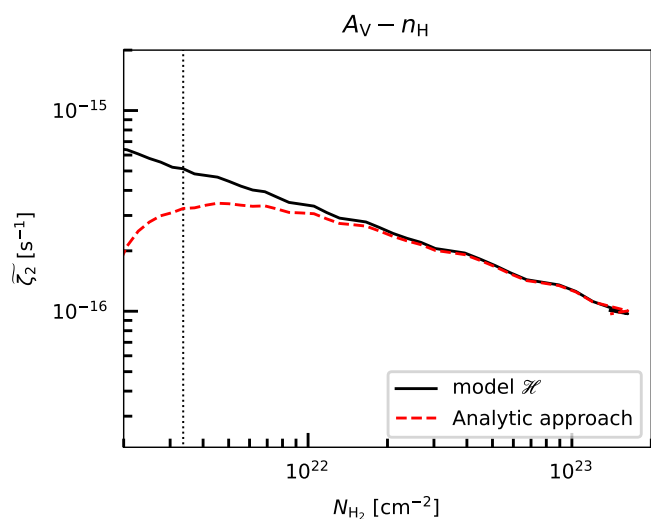


**Fig. 3.** Comparison of the calculated CRIR from the analytic approach ( $\zeta_2$ , red dashed curve) and the CR attenuation model (black solid curve). The vertical dashed line represents the 50% deviation between the analytic approach and the CR attenuation model.

parable or lower abundances than that of HD. Thus, the main destruction channels of  $\text{H}_3^+$  we considered in Sect. 2 would change. The results suggest that our analytic approach may only give a lower limit for metal-poor starburst galaxies where the CRIR is supposed to be extremely high.

#### 4.1.2. Variation of source size

In our simulations, we set the cloud radius to be 1 pc. In reality, the size of the source could change significantly in different environments. Figure 2 shows the deviation maps from 3D-PDR simulations, where the analytic approach gives a good estimation of CRIR for  $A_V \gtrsim 4$  mag. This value corresponds to 0.25 pc at  $n_H = 10^4 \text{ cm}^{-3}$  and  $2.5 \times 10^{-3}$  pc ( $\sim 500$  AU) at  $n_H = 10^6 \text{ cm}^{-3}$ , suggesting a minimal source size that the analytic approach can give a good CRIR estimation. We also run simulations with two different source sizes ( $r = 0.1, 5$  pc) in UCLHEM. As seen in Fig. 7, changing the source size has no impact on the conclusions.

#### 4.1.3. HMC models

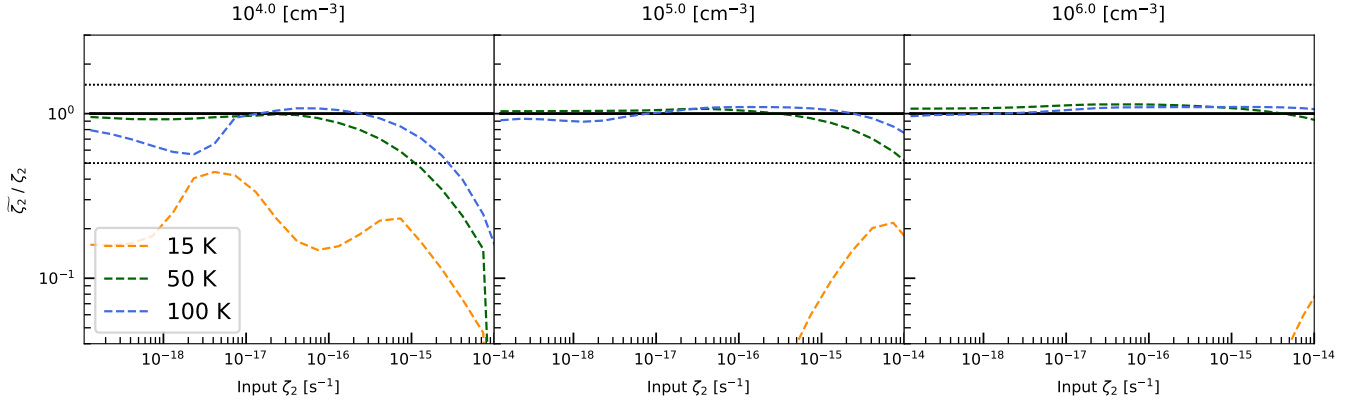
To test the robustness of our analytic approach, we perform tests with more physical HMC models, which consider both the variation of density and temperature with evolution timescale. Each of the HMC models consists of two stages. In the first stage, we perform simulations of the isothermal free-fall collapse (representing a prestellar phase) with an initial temperature of 10 K. The free-fall collapse phase starts from a cloud with  $n_H = 10^3 \text{ cm}^{-3}$ , reaching higher densities ( $n_H^{\text{final}} = 10^4, 10^5$ , and  $10^6 \text{ cm}^{-3}$ ) at a free-fall timescale<sup>7</sup> (see Priestley et al. 2018, for a detailed description of the density profiles in collapse models). In the second stage, we perform simulations with a gradually increasing gas temperature (representing a formed HMPO or HMC) due to the heating of a central massive star. The gas densities and initial composition of all the species in the second stage inherit from the final state of the free-fall collapse. The mass of the central star in the HMC model is set to  $10 M_\odot$ , and the gas temperature increases from 10 K to 200 K within a few  $10^5$  yr (see Viti et al. 2004 and Awad et al. 2010 for more details of the treatment of temperature).

Figure 8 shows the comparison between the analytic approach and the HMC models. The analytic approach gives a reasonable estimation for all models at  $\zeta_2 \geq 10^{-17} \text{ s}^{-1}$ , while it underestimates  $\zeta_2$  by up to a factor of 25 at  $\zeta_2 \approx 10^{-18} \text{ s}^{-1}$ . As shown in Fig. A.1 this is due to an underestimation of electron abundance through Eq. 2 at very low CRIR, where the formation of ions (e.g.,  $\text{HCO}^+$  and  $\text{N}_2\text{H}^+$ ) is suppressed while Eq. 2 does not consider the contribution from other ions such as  $\text{C}^+$ ,  $\text{Mg}^+$ , etc.

#### 4.2. Uncertainties

There are a few factors that may bring uncertainties when using the analytic approach to calculate the CRIR. The most uncertain factors are the assumption of the gas phase abundances of O and  $\text{N}_2$ , since they are almost undetectable in dense clouds. On the other hand, when there is a lack of measurements of CO isotopologues, a CO abundance of  $10^{-4}$  (without depletion) is frequently assumed. In this section, we discuss the uncertainties induced by these factors.

<sup>7</sup> The choice of the initial density would not influence the conclusion but could greatly reduce the time cost of each simulation.



**Fig. 4.** Comparison between our approach and the UCLCHEM simulations. The x-axis denotes the input CRIR of each simulation, where the CRIR in each simulation is treated as uniform. The y-axis denotes the ratio between the calculated CRIR and the input one ( $\bar{\zeta}_2/\zeta_2$ ) at  $t = 10^6$  yr. The black horizontal line represents the fiducial value, and the horizontal dotted lines represent 50% of the deviation from the input values. Orange, green, and blue dashed lines represent results at  $T_k = 15, 50,$  and  $100$  K. Columns from left to right represent simulations with the cloud densities  $n_H = 10^4, 10^5,$  and  $10^6$   $\text{cm}^{-3}$ . The large deviation at 15 K is due to the freeze-out processes that greatly reduce the gas-phase abundances of key species such as CO, thus, the chemical reactions we described in Sect. 2.1 are no longer satisfied.

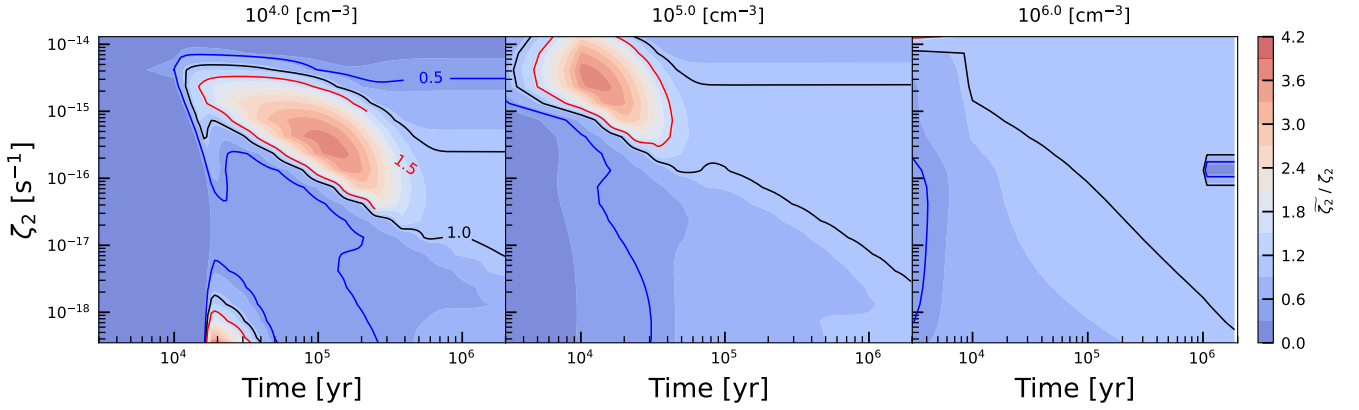


**Fig. 5.** The deviation between the analytic approaches and the input values at different evolution timescales and  $\zeta_2$ . Red, black, and blue curves denote the 50%, 0%, and -50% deviations.

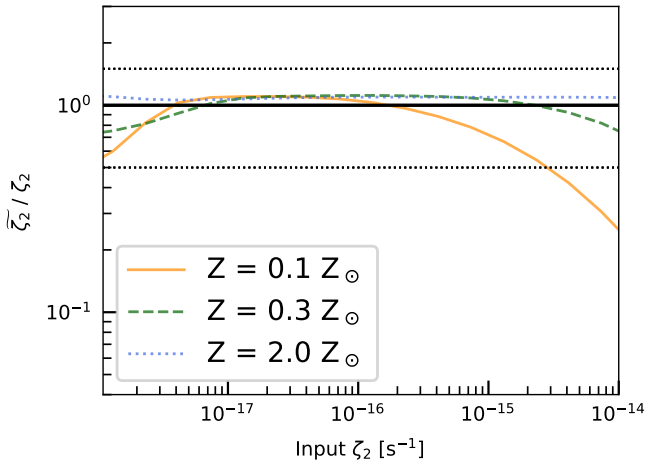


**Fig. 6.** The comparison between our approach and UCLCHEM simulations under different metallicities ( $Z$ ). The temperature and density are adopted as 100 K and  $10^6$   $\text{cm}^{-3}$ . The solid, dash, and dotted lines represent  $Z = 0.1, 0.3,$  and  $2 Z_\odot$ . The black horizontal line represents the fiducial value, and the horizontal dotted lines represent 50% of the deviation from the input values.

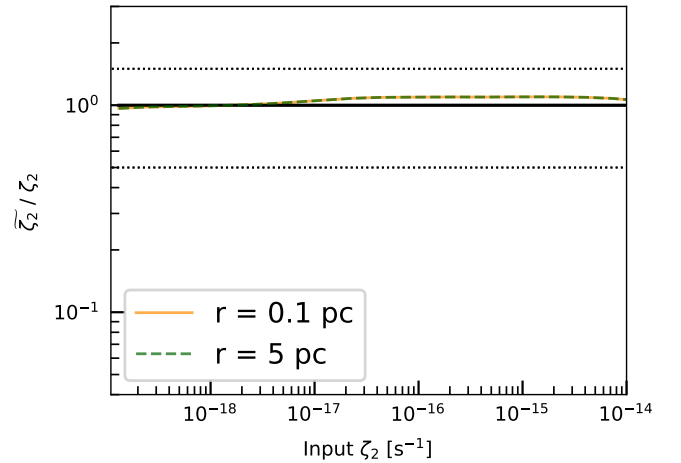


**Fig. 7.** The comparison between our approach and UCLCHEM simulations under different source size ( $r = 0.1$  and  $5$  pc). The temperature and density are adopted as 100 K and  $10^6$   $\text{cm}^{-3}$ . The solid and dash lines represent  $r = 0.1$  and  $5$  pc, respectively. The black horizontal line represents the fiducial value, and the horizontal dotted lines represent 50% of the deviation from the input values.

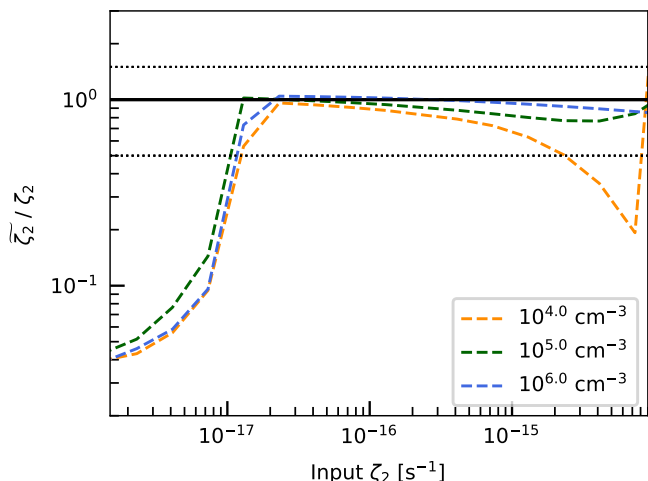


**Fig. 8.** Comparison of  $\bar{\zeta}_2/\zeta_2$  as a function of the input  $\zeta_2$  in the HMC models. Orange, green, and blue lines represent results at  $n_{\text{H}} = 10^4, 10^5, 10^6 \text{ cm}^{-3}$ . Dashed horizontal lines represent the 50% deviation from the input values.

Without depletion, most of the carbon is found in CO molecules in dense molecular clouds. Thus, CO has been widely used as an indicator of  $\text{H}_2$  in large surveys (Dame et al. 2001; Su et al. 2019). The canonical abundance of CO in well-shielded molecular clouds (e.g.,  $A_{\text{V}} > 4 \text{ mag}$ ) is  $\approx 10^{-4}$  (Frerking et al. 1982; Pineda et al. 2010; Luo et al. 2023a). The calculated abundances of CO toward specific sightlines could also be biased by the method of deriving the column densities, excitation, and optical depths.

The abundance of molecular oxygen ( $\text{O}_2$ ) from both observations and chemical models is negligible compared with atomic oxygen in dense clouds (Larsson et al. 2007; Goldsmith et al. 2011; Wakelam et al. 2019). Thus, the majority of the oxygen element should be in the atomic form in dense clouds. The measured mean value of atomic oxygen abundance (with respect to total H) in the moderate density cloud ( $n_{\text{H}_2} = \text{a few } 10^4 \text{ cm}^{-3}$ ) is  $(2.51 \pm 0.69) \times 10^{-4}$  (Lis et al. 2023).

Since there are no observable rotational or vibrational transitions of  $\text{N}_2$  in dense clouds, the main reservoir of nitrogen in molecular clouds is still under debate (Womack et al. 1992; Maret et al. 2006; Furuya & Persson 2018). Measurements from  $\text{N}_2\text{H}^+$  in different environments suggest that  $\text{N}_2$  should be abundant in dense regions (Womack et al. 1992; Furuya & Persson 2018).

To examine the uncertainties of CRIR induced by CO and O abundances, and whether the assumed abundances of  $\text{N}_2$  are reasonable, we calculate the CRIR for each of the above chemical simulations, with the abundances (with respect to total H, including the uncertainties) of CO, O, and  $\text{N}_2$  to be  $(1.0 \pm 0.3) \times 10^{-4}$ ,  $(2.51 \pm 0.69) \times 10^{-4}$ , and  $(3.8 \pm 0.5) \times 10^{-5}$ .

Figure 9 shows the mean value (dashed lines) and  $1\sigma$  deviation (shadow regions) of our analytic approach with comparison to the input  $\zeta_2$  from 3D-PDR, isothermal simulations from UCLCHEM, and HMC simulations from UCLCHEM, respectively. As can be seen, the derived mean values of CRIR are mostly within 50% deviation for 3D-PDR and HMC simulations with UCLCHEM even if we consider the uncertainties induced by CO, O, and N, and the results in Sect. 3 remain the same.

Larger differences can be found in isothermal simulations with UCLCHEM. For high-temperature models ( $T_{\text{k}} = 50, 100 \text{ K}$ )

with  $\zeta_2$  between  $10^{-17}$  to  $10^{-14} \text{ s}^{-1}$ , the mean value is consistent with that of Fig. 4 and the deviation induced by the above uncertainties are mostly within 50%. When  $\zeta_2$  below a few  $10^{-18} \text{ s}^{-1}$ , the deviation induced by the above uncertainties would tend to decrease the calculated CRIR by up to a factor of  $\sim 10$ . The results suggest that the assumed initial abundances of O or  $\text{N}_2$  deviate from the simulations at low CRIR. For low-temperature models ( $T_{\text{k}} = 15 \text{ K}$ ), the predicted mean value is significantly different from the previous results in Fig. 4, suggesting an unpredictable behavior at the low temperature and the analytic approach should not be used in such environments. In the following analysis, we consider all the above uncertainties when calculating the CRIR using Eq. 11.

#### 4.3. Comparison between our calculations and the literature

We apply our method to some well-known sources with reported CRIR values found in the literature.

##### 4.3.1. OMC-2 FIR 4

At a distance of  $\sim 420 \text{ pc}$  (Hirota et al. 2007), OMC-2 FIR 4 is located in the north of the Orion KL object, which hosts a few embedded low- and intermediate-mass protostars (Shimajiri et al. 2008). Multi-transitions of  $\text{N}_2\text{H}^+$  ( $J=6-5$  to  $12-11$ ),  $\text{HCO}^+$  ( $J=6-5$  to  $13-12$ ), and  $\text{H}^{13}\text{CO}^+$  ( $J=6-5$  to  $7-6$ ) have been observed toward this source with *Herschel*. The detailed spectral line energy distribution (SLED) analysis can be found in Ceccarelli et al. (2014b).

The non-local thermal equilibrium (LTE) results for the warm core component and the envelope are taken from Table 1 in Ceccarelli et al. (2014b). The column density of  $\text{H}_2$  ( $N_{\text{H}_2}$ ) has relatively larger uncertainties than those of molecular lines. The value of  $N_{\text{H}_2}$  derived from the modeled source size ( $\sim 1600 \text{ AU}$ ) in Ceccarelli et al. (2014b) is  $9.6 \times 10^{23} \text{ cm}^{-2}$ . However, this value is higher than that given by radiative transfer modeling of dust spectral energy distribution (SED,  $N_{\text{H}_2} = 2.2 \times 10^{23} \text{ cm}^{-2}$ , Crimier et al. 2009) and that measured from 3 mm continuum ( $1-9 \times 10^{23} \text{ cm}^{-2}$ , Fontani et al. 2017). In regards to the 3 mm continuum, which could be contributed by both free-free emission and dust thermal emission, the derived  $N_{\text{H}_2}$  should be considered as an upper limit.

On the other hand, due to the lack of velocity information in the dust continuum, the core and envelope components cannot be distinguished. To simplify our calculations, a median value of  $N_{\text{H}_2} = (5 \pm 1.3) \times 10^{23} \text{ cm}^{-2}$  is adopted for the warm core component (which is the dominant component). The minimum and maximum values of  $N_{\text{H}_2}$  adopted are  $1 \times 10^{23} \text{ cm}^{-2}$  and  $9 \times 10^{23} \text{ cm}^{-2}$ , respectively. For the envelope component, the value of  $N_{\text{H}_2} = 6.6 \times 10^{22} \text{ cm}^{-2}$  is adopted according to the models presented in Ceccarelli et al. (2014b).

Following Eq. 11, the derived CRIR toward the warm core component is  $\zeta_2 = (1.0 \pm 0.3) \times 10^{-14} \text{ s}^{-1}$ , with a lower limit of  $(0.6 \pm 0.2) \times 10^{-14} \text{ s}^{-1}$  (adopting  $N_{\text{H}_2} = 9 \times 10^{23} \text{ cm}^{-2}$ ) and an upper limit of  $(5.2 \pm 1.4) \times 10^{-14} \text{ s}^{-1}$  (adopting  $N_{\text{H}_2} = 1 \times 10^{23} \text{ cm}^{-2}$ ). The models of Ceccarelli et al. (2014b) result in a CRIR more than two orders of magnitude higher than ours (they find  $\zeta_2 \sim 6 \times 10^{-12} \text{ s}^{-1}$ ). We argue that this may be related to their overestimation of  $\text{N}_2\text{H}^+$  and  $\text{HCO}^+$  abundances by 2–3 orders of magnitude. According to the non-LTE analysis in Ceccarelli et al. (2014b), the calculated abundances of  $\text{HCO}^+$  and  $\text{N}_2\text{H}^+$  should be  $7.3 \times 10^{-11}$  and  $3.1 \times 10^{-11}$ , respectively. However, the

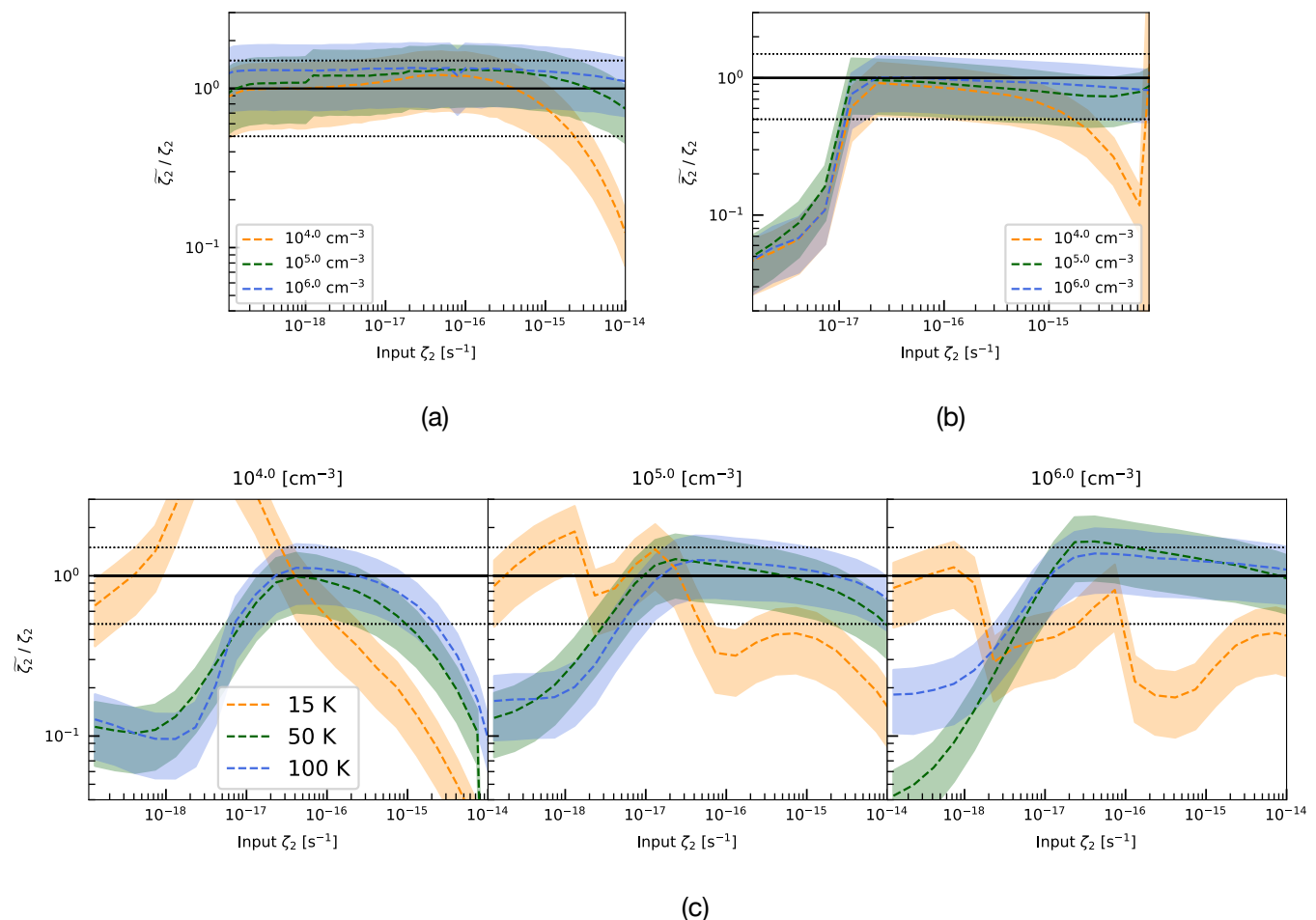


**Fig. 9.** Comparison of  $\tilde{\zeta}_2/\zeta_2$  and uncertainties induced by gas phase abundances of CO, O, and N<sub>2</sub> for (a) 3D-PDR simulations, (b) HMC simulations from UCLCHEM, and (c) isothermal cloud simulations from UCLCHEM. The dashed curves and the shadow regions represent the mean value and  $1\sigma$  deviation from our calculation. Orange, green, and blue lines represent different densities (in (a) and (b)) or temperatures (in (c)). Dashed horizontal lines represent 50% deviation from the input  $\zeta_2$ .

resultant abundances of HCO<sup>+</sup> and N<sub>2</sub>H<sup>+</sup> from their chemistry analysis are  $10^{-7}$  and  $3 \times 10^{-8}$ .

The derived CRIR toward the envelope is  $\zeta_2 = (1.0 \pm 0.3) \times 10^{-14} \text{ s}^{-1}$ , which is slightly lower than the value given by Ceccarelli et al. (2014b,  $\zeta_2 = 1.5\text{--}8 \times 10^{-14} \text{ s}^{-1}$ ) and recent chemical modeling from carbon-chain molecules ( $\zeta_2 \approx 4 \times 10^{-14} \text{ s}^{-1}$ , Fontani et al. 2017; Favre et al. 2018).

#### 4.3.2. L1157-B1

L1157-B1 is a well-known line-rich shock region, which is located at the blue-shifted outflow lobe of a low-mass protostar L1157 (Bachiller & Pérez Gutiérrez 1997; Lefloch et al. 2017; Holdship et al. 2019; Codella et al. 2020). Various molecular line emissions (e.g., CH<sub>3</sub>OH, SiO) have been detected toward L1157-B1 with broad linewidth (a few to  $\sim 20 \text{ km s}^{-1}$ ) and enhanced abundance respect to H<sub>2</sub>. High sensitivity IRAM 30-m observations found broad linewidth ( $4.3 \pm 0.2 \text{ km s}^{-1}$ ) emission of N<sub>2</sub>H<sup>+</sup>, while the calculated abundance of N<sub>2</sub>H<sup>+</sup> has large uncertainties due to the unknown kinetic temperature (Codella et al. 2013; Podio et al. 2014).

Recent NH<sub>3</sub> observations by JVLA have revealed the distribution of  $T_k$  at the blue-shifted lobe of L1157 (Feng et al. 2022). In the B1 regions,  $T_k$  is in the range of 80–120 K. We take an average  $T_k$  to be 100 K within the 26'' IRAM beam-

size toward L1157-B1, and a consistent  $n_{\text{H}_2}$  of  $10^5 \text{ cm}^{-3}$  as in Podio et al. (2014). We use the non-local thermal equilibrium (LTE) radiative transfer model RADEX (van der Tak et al. 2007) to calculate the column density. The collisional excitation rate coefficients of N<sub>2</sub>H<sup>+</sup> from Daniel et al. (2005) are adopted and obtained from the Leiden Atomic and Molecular Database (LAMDA, Schöier et al. 2005). The derived column density of N<sub>2</sub>H<sup>+</sup> is  $(9.2 \pm 1.0) \times 10^{11} \text{ cm}^{-2}$ , and the resultant abundance is  $(9.2 \pm 1.0) \times 10^{-10}$ . The abundances of CO and HCO<sup>+</sup> are  $1 \times 10^{-4}$  and  $7 \times 10^{-9}$ , respectively (Podio et al. 2014). The derived CRIR toward L1157-B1 from Eq. 11 is  $\zeta_2 = (2.2 \pm 0.4) \times 10^{-16} \text{ s}^{-1}$ , which is in good agreement with the value from chemical modeling ( $\zeta_2 \approx 3 \times 10^{-16} \text{ s}^{-1}$ , Podio et al. 2014; Benedettini et al. 2021).

## 5. The CRIR in HMSFRs

To statistically investigate how the CRIR varies in different stages of HMSFRs, we calculate CRIR using our method toward a total of 82 samples from Purcell et al. (2006, 2009), Gerner et al. (2014, 2015), and Entekhabi et al. (2022). These samples include 20 HMPOs, 54 HMCs, and 8 ultra-compact H II (UCH II) regions.

In the hot core samples of Purcell et al. (2006, 2009), the gas temperatures are in the range of  $28 \pm 7$  to  $131 \pm 53 \text{ K}$ , which



are derived from the rotational diagram of CH<sub>3</sub>CN. The column densities of HCO<sup>+</sup> are derived from the optically thin H<sup>13</sup>CO<sup>+</sup> emission, assuming  $^{12}\text{C}/^{13}\text{C} = 50$  and  $T_{\text{ex}} = 50$  K. The column densities of N<sub>2</sub>H<sup>+</sup> are derived from the hyperfine transitions with the assumption of  $T_{\text{ex}} = 10$  K and are corrected for the beam dilution with dust continuum. The column and volume densities of H<sub>2</sub> are derived from 1.2 mm continuum emission (see Purcell et al. (2009) for details). There are no observations of CO isotopologues, in our calculation, a constant abundance of CO ( $1.0 \pm 0.3 \times 10^{-4}$ ) is assumed for all the hot core samples from Purcell et al. (2006, 2009).

In the samples of Gerner et al. (2014, 2015), the gas temperatures of HMPOs, HMCs, and UCH II are 29.5, 40.2, and 36 K, respectively. The column densities of HCO<sup>+</sup> are derived from two transitions of H<sup>13</sup>CO<sup>+</sup> (1–0 and 3–2) using RADEX, assuming  $^{12}\text{C}/^{13}\text{C} = 89^8$ . The column densities of N<sub>2</sub>H<sup>+</sup> are calculated with the hyperfine structure fitting routine. The column densities of CO are derived from C<sup>18</sup>O with LTE, assuming  $^{16}\text{O}/^{18}\text{O} = 500$ . The H<sub>2</sub> column densities are derived from dust emission at 850  $\mu\text{m}$  with JCMT or 1.2 mm with IRAM-30m (see Gerner et al. (2014) for details). The volume densities of H<sub>2</sub> are derived by assuming a typical source size of 0.5 pc for all sources. We note that the choice of source size is based on the IRAM-30 m beam size, which may underestimate the actual physical size of these systems. Thus, the derived CRIR may also be underestimated.

Figure 10 shows the calculated  $\zeta_2$  from the above samples. For comparison, the CRIR values from L1544 (Redaelli et al. 2021) and IRDC G28.37+00.07 (Entekhabi et al. 2022), and the theoretical CR attenuation models  $\mathcal{L}$ ,  $\mathcal{H}$ , and  $\mathcal{U}$  from Padovani et al. (2024) are also overlaid. The models  $\mathcal{L}$ ,  $\mathcal{H}$ , and  $\mathcal{U}$  are based on different assumptions on the low-energy slope of the interstellar CR proton spectrum (see Ivlev et al. (2015) and Padovani et al. (2024) for a detailed description of the parameterization of the CR spectrum), which have energy density  $\varepsilon_{\text{CR}} \approx 0.65, 1.18$  and  $2.28$  eV cm<sup>-3</sup>, respectively. The trends of the CRIR in Fig. 10 also account for the ionization due to primary and secondary electrons. It is noted that all the physical parameters ( $T_{\text{kin}} \geq 30$  K,  $n_{\text{H}_2} > 10^4$  cm<sup>-3</sup>, no CO depletion) are within the allowable parameter space that the analytic approach gives a good approximation. The average values of  $\zeta_2$  in HMPOs, HMCs, and UCH II are  $(2.5 \pm 1.3) \times 10^{-16}$ ,  $(7.4 \pm 5.0) \times 10^{-16}$ , and  $(3.4 \pm 3.4) \times 10^{-16}$  s<sup>-1</sup>, respectively. The values in these targets are over an order of magnitude higher than the measurements in prestellar cores (e.g., L1544 and G28.37+00.07) and that predicted by the model  $\mathcal{H}$ , where the latter describes the average decrease of the observationally estimated  $\zeta_2$  (Padovani et al. 2022; Padovani 2023).

Interestingly, observations from *Fermi* and LHAASO also find the ubiquitous  $\gamma$ -ray emissions in HMSFRs (e.g., W43) from sub-GeV to PeV (Yang et al. 2018; Yang & Wang 2020; Vink 2022; de la Fuente et al. 2023), suggesting an efficient acceleration of particles in active star-forming environments (Bykov et al. 2020; Tibaldo et al. 2021; Owen et al. 2023). While the high energy ( $E \gg 10$  GeV)  $\gamma$ -ray could originate from CRs accelerated by stellar wind of massive stars (Peron et al. 2024), the lower energy  $\gamma$ -ray could come from the embedded massive protostars which undergo their accretion phase and in which the first-order Fermi acceleration mechanism operates, e.g., jet shocks (Padovani et al. 2015, 2016; Lattanzi et al. 2023), shocks

on protostellar surfaces (Padovani et al. 2015, 2016; Gaches & Offner 2018), H II regions (Padovani et al. 2019; Meng et al. 2019), and wind-driven shocks (Bhadra et al. 2022). These processes would accelerate CRs to tens of GeV (depending on the actual physical conditions), leading to a detectable  $\gamma$ -ray emission toward individual protostar (Araudo et al. 2007; Bosch-Ramon et al. 2010; Padovani et al. 2015, 2016). The detection of  $\gamma$ -ray emission at  $\sim 1$  GeV from the protostellar jet in HH 80-81 and  $\sim 10$  GeV level toward a young massive protostar supports these scenarios (Yan et al. 2022; de Oña Wilhelmi et al. 2023).

The high values of  $\zeta_2$  from our work are also consistent with the model prediction under the existence of internal CR source models as presented by Gaches et al. (2019), in which the CRIR is in the range of  $10^{-16}$  s<sup>-1</sup> to  $10^{-14}$  s<sup>-1</sup> at a column density of  $\sim 10^{23}$  cm<sup>-2</sup>. In addition, observations toward B335 also suggest high CRIR near the central protostars (Cabedo et al. 2023). The increasing trend of CRIR from HMPOs to HMCs is consistent with our understanding that HMCs are in a more evolved phase and that star-formation activities (e.g., shocks) in HMCs may have stronger impacts on the surrounding gas. At the late stage of HMSFRs, once the central massive protostars have gathered enough mass and evolved to the zero age main sequence, the stellar wind and radiation feedback would drive the surrounding gas and lead to an expansion of UCH II regions. And because the accretion and outflows/jets gradually disappear in the late stage, the CRIR could be lower.

Such a methodology could be, in principle, used to estimate CRIR of external galaxies, where the physical properties could be quite different to those in the Milky Way (Rosolowsky et al. 2021). However, we should note that a better understanding of the source properties (e.g., density, metallicity) and a correction for the beam dilution are needed before using such a method on distant starburst galaxies. This is because, the spatial resolution of distant galaxies is usually quite low, thus, the average volume density within the beam is not supposed to be high enough to give a good approximation at very high CRIR ( $\zeta_2 \geq 10^{-14}$  s<sup>-1</sup>, see Sect. 3). For cosmic noon starburst galaxies where the CRIR is supposed to be extremely high (e.g., orders of magnitude above  $\sim 10^{-16} - 10^{-14}$  s<sup>-1</sup>, Indriolo et al. 2018), the analytic approach could only give a lower limit.

## 6. Conclusions

We present a new analytic approach to estimate the CRIR using the abundances of HCO<sup>+</sup>, N<sub>2</sub>H<sup>+</sup>, and CO. The basic assumptions of deriving the analytic approach are: 1) HCO<sup>+</sup>, N<sub>2</sub>H<sup>+</sup>, H<sub>3</sub><sup>+</sup>, and H<sub>3</sub>O<sup>+</sup> are the main ions, and 2) warm gas environments (depletion of molecules can be ignored). Our analytic approach has been tested with different 3D-PDR and UCLCHEM simulations. The main conclusions are as follows:

1. The analytic approach gives a reasonable estimation of  $\zeta_2$  (to within 50% deviation) in dense warm gas (e.g.,  $n_{\text{H}} \geq 10^4$  cm<sup>-3</sup>,  $T \geq 50$  K) for  $A_{\text{V}} \geq 4$  mag,  $t \geq 2 \times 10^4$  yr. The higher the gas density, the better the estimation from our analytic approach. Such environments may correspond to HMPOs and HMCs.
2. Application of our method to the OMC-2 FIR 4 envelope and L1157-B1 results in  $\zeta_2$  values of  $(1.0 \pm 0.3) \times 10^{-14}$  s<sup>-1</sup> and  $(2.2 \pm 0.4) \times 10^{-16}$  s<sup>-1</sup>, which are in good agreement with the estimation of  $\zeta_2$  from the chemical modeling in the literature, suggesting wide applicability of our method in warm gas environments.

<sup>8</sup> Although the adopted value is higher than the local ISM ( $\sim 65$ , Milam et al. 2005) and those from Purcell et al. (2006, 2009), a variance of  $^{12}\text{C}/^{13}\text{C}$  by 30% would only result in an uncertainty of  $\zeta_2$  by  $\sim 1\%$ .

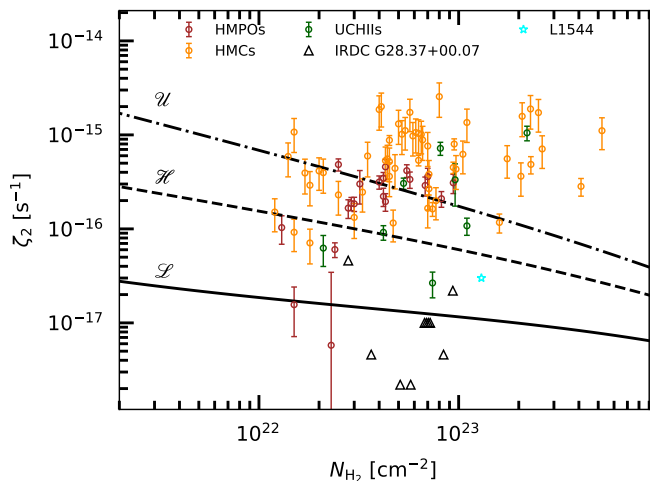


**Fig. 10.** The calculated  $\zeta_2$  toward HMPOs (brown), HMCs (orange), and UCH IIs (green). Black triangles represent CRIR from IRDC G28.37+00.07, which are taken from Entekhabi et al. (2022). The cyan star represents CRIR from prestellar core L1544, which is taken from Redaelli et al. (2021). The black solid, dashed, and dash-dotted curves denote the theoretical CR attenuation models  $\mathcal{L}$ ,  $\mathcal{H}$ , and  $\mathcal{U}$  by Padovani et al. (2024).

- The values of  $\zeta_2$  toward a total of 82 samples of HMPOs, HMCs, and UCH II have been derived with our analytic approach. The average value of  $\zeta_2$  in HMCs is over an order of magnitude higher than the prediction of canonical CR attenuation models. Our results suggest that the internal massive protostars are likely to be responsible for the high CRIR.

Future high spatial resolution interferometry observations with multi-transitions of molecular lines will allow the more robust estimation and direct mapping of CRIR in HMSFRs, which is helpful to understand the origin of the high CRIR (Padovani et al. 2019, 2021).

*Acknowledgements.* We thank Evelyne Roueff for her careful review of the chemical reactions in our manuscript, particularly for pointing out that the endothermic reaction can only occur under specific conditions. BALG acknowledges support from a Chalmers Cosmic Origins postdoctoral fellowship.

## References

Araudo, A. T., Romero, G. E., Bosch-Ramon, V., & Paredes, J. M. 2007, *A&A*, 476, 1289  
 Awad, Z., Viti, S., Collings, M. P., & Williams, D. A. 2010, *MNRAS*, 407, 2511  
 Bachiller, R. & Pérez Gutiérrez, M. 1997, *ApJ*, 487, L93  
 Benedettini, M., Viti, S., Codella, C., et al. 2021, *A&A*, 645, A91  
 Beuther, H., Churchwell, E. B., McKee, C. F., & Tan, J. C. 2007a, in *Protostars and Planets V*, ed. B. Reipurth, D. Jewitt, & K. Keil, 165  
 Beuther, H., Schilke, P., Menten, K. M., et al. 2002a, *ApJ*, 566, 945  
 Beuther, H., Schilke, P., Sridharan, T. K., et al. 2002b, *A&A*, 383, 892  
 Beuther, H., Zhang, Q., Bergin, E. A., et al. 2007b, *A&A*, 468, 1045  
 Bhadra, S., Gupta, S., Nath, B. B., & Sharma, P. 2022, *MNRAS*, 510, 5579  
 Bialy, S. 2020, *Communications Physics*, 3, 32  
 Bialy, S., Belli, S., & Padovani, M. 2022, *A&A*, 658, L13  
 Bialy, S. & Sternberg, A. 2015, *MNRAS*, 450, 4424  
 Bisbas, T. G., Bell, T. A., Viti, S., Yates, J., & Barlow, M. J. 2012, *MNRAS*, 427, 2100  
 Bisbas, T. G., Papadopoulos, P. P., & Viti, S. 2015, *ApJ*, 803, 37  
 Bisbas, T. G., van Dishoeck, E. F., Hu, C.-Y., & Schrupa, A. 2023, *MNRAS*, 519, 729  
 Bisbas, T. G., van Dishoeck, E. F., Papadopoulos, P. P., et al. 2017, *ApJ*, 839, 90  
 Blake, G. A., Sutton, E. C., Masson, C. R., & Phillips, T. G. 1987, *ApJ*, 315, 621  
 Bosch-Ramon, V., Romero, G. E., Araudo, A. T., & Paredes, J. M. 2010, *A&A*, 511, A8

Bovino, S., Ferrada-Chamorro, S., Lupi, A., Schleicher, D. R. G., & Caselli, P. 2020, *MNRAS*, 495, L7  
 Bykov, A. M., Marcowith, A., Amato, E., et al. 2020, *Space Sci. Rev.*, 216, 42  
 Cabedo, V., Maury, A., Girart, J. M., et al. 2023, *A&A*, 669, A90  
 Caselli, P., Sipilä, O., & Harju, J. 2019, arXiv e-prints, arXiv:1905.08653  
 Caselli, P., Walmsley, C. M., Terziva, R., & Herbst, E. 1998, *ApJ*, 499, 234  
 Ceccarelli, C., Caselli, P., Bockelée-Morvan, D., et al. 2014a, in *Protostars and Planets VI*, ed. H. Beuther, R. S. Klessen, C. P. Dullemond, & T. Henning, 859–882  
 Ceccarelli, C., Dominik, C., López-Sepulcre, A., et al. 2014b, *ApJ*, 790, L1  
 Codella, C., Ceccarelli, C., Bianchi, E., et al. 2020, *A&A*, 635, A17  
 Codella, C., Viti, S., Ceccarelli, C., et al. 2013, *ApJ*, 776, 52  
 Crimier, N., Ceccarelli, C., Lefloch, B., & Faure, A. 2009, *A&A*, 506, 1229  
 Dalgarno, A. 2006, *Proceedings of the National Academy of Science*, 103, 12269  
 Dame, T. M., Hartmann, D., & Thaddeus, P. 2001, *ApJ*, 547, 792  
 Daniel, F., Dubernet, M. L., Meuwly, M., Cernicharo, J., & Pagani, L. 2005, *MNRAS*, 363, 1083  
 de la Fuente, E., Toledano-Juarez, I., Kawata, K., et al. 2023, *PASJ*, 75, 546  
 de Oña Wilhelmi, E., López-Coto, R., & Su, Y. 2023, *MNRAS*, 523, 105  
 Entekhabi, N., Tan, J. C., Cosentino, G., et al. 2022, *A&A*, 662, A39  
 Favre, C., Ceccarelli, C., López-Sepulcre, A., et al. 2018, *ApJ*, 859, 136  
 Feng, S., Liu, H. B., Caselli, P., et al. 2022, *ApJ*, 933, L35  
 Fontani, F., Ceccarelli, C., Favre, C., et al. 2017, *A&A*, 605, A57  
 Frerking, M. A., Langer, W. D., & Wilson, R. W. 1982, *ApJ*, 262, 590  
 Friedman, S. D., Chayer, P., Jenkins, E. B., et al. 2023, *ApJ*, 946, 34  
 Furuya, K. & Persson, M. V. 2018, *MNRAS*, 476, 4994  
 Gaches, B. A. L., Bialy, S., Bisbas, T. G., et al. 2022a, *A&A*, 664, A150  
 Gaches, B. A. L., Bisbas, T. G., & Bialy, S. 2022b, *A&A*, 658, A151  
 Gaches, B. A. L. & Offner, S. S. R. 2018, *ApJ*, 861, 87  
 Gaches, B. A. L., Offner, S. S. R., & Bisbas, T. G. 2019, *ApJ*, 878, 105  
 Gerin, M., de Luca, M., Black, J., et al. 2010, *A&A*, 518, L110  
 Gerner, T., Beuther, H., Semenov, D., et al. 2014, *A&A*, 563, A97  
 Gerner, T., Shirley, Y. L., Beuther, H., et al. 2015, *A&A*, 579, A80  
 Glassgold, A. E. & Langer, W. D. 1973, *ApJ*, 179, L147  
 Goldsmith, P. F., Liseau, R., Bell, T. A., et al. 2011, *ApJ*, 737, 96  
 Herbst, E. & van Dishoeck, E. F. 2009, *ARA&A*, 47, 427  
 Hincelin, U., Wakelam, V., Hersant, F., et al. 2011, *A&A*, 530, A61  
 Hirota, T., Bushimata, T., Choi, Y. K., et al. 2007, *PASJ*, 59, 897  
 Holdship, J., Jimenez-Serra, I., Viti, S., et al. 2019, *ApJ*, 878, 64  
 Holdship, J., Viti, S., Jiménez-Serra, I., Makrymallis, A., & Priestley, F. 2017, *AJ*, 154, 38  
 Indriolo, N. 2023, *ApJ*, 950, 64  
 Indriolo, N., Bergin, E. A., Falgarone, E., et al. 2018, *ApJ*, 865, 127  
 Indriolo, N. & McCall, B. J. 2012, *ApJ*, 745, 91  
 Indriolo, N., Neufeld, D. A., Gerin, M., et al. 2015, *ApJ*, 800, 40  
 Ivlev, A. V., Padovani, M., Galli, D., & Caselli, P. 2015, *ApJ*, 812, 135  
 Kurtz, S., Cesaroni, R., Churchwell, E., Hofner, P., & Walmsley, C. M. 2000, in *Protostars and Planets IV*, ed. V. Mannings, A. P. Boss, & S. S. Russell, 299–326  
 Larsson, B., Liseau, R., Pagani, L., et al. 2007, *A&A*, 466, 999  
 Lattanzi, V., Alves, F. O., Padovani, M., et al. 2023, *A&A*, 671, A35  
 Lefloch, B., Ceccarelli, C., Codella, C., et al. 2017, *MNRAS*, 469, L73  
 Linsky, J. L., Draine, B. T., Moos, H. W., et al. 2006, *ApJ*, 647, 1106  
 Lis, D. C., Goldsmith, P. F., Güsten, R., et al. 2023, *A&A*, 669, L15  
 Luo, G., Feng, S., Li, D., et al. 2019, *ApJ*, 885, 82  
 Luo, G., Zhang, Z.-Y., Bisbas, T. G., et al. 2023a, *ApJ*, 942, 101  
 Luo, G., Zhang, Z.-Y., Bisbas, T. G., et al. 2023b, *ApJ*, 946, 91  
 Majumdar, L., Gratier, P., Ruaud, M., et al. 2017, *MNRAS*, 466, 4470  
 Maret, S., Bergin, E. A., & Lada, C. J. 2006, *Nature*, 442, 425  
 McElroy, D., Walsh, C., Markwick, A. J., et al. 2013, *A&A*, 550, A36  
 Meng, F., Sánchez-Monge, Á., Schilke, P., et al. 2019, *A&A*, 630, A73  
 Meyer, D. M., Cardelli, J. A., & Sofia, U. J. 1997, *ApJ*, 490, L103  
 Meyer, D. M., Jura, M., & Cardelli, J. A. 1998, *ApJ*, 493, 222  
 Milam, S. N., Savage, C., Brewster, M. A., Ziurys, L. M., & Wyckoff, S. 2005, *ApJ*, 634, 1126  
 Millar, T. J., Bennett, A., & Herbst, E. 1989, *ApJ*, 340, 906  
 Millar, T. J., Walsh, C., Van de Sande, M., & Markwick, A. J. 2024, *A&A*, 682, A109  
 Motte, F., Bontemps, S., & Louvet, F. 2018, *ARA&A*, 56, 41  
 Neufeld, D. A. & Wolfire, M. G. 2017, *ApJ*, 845, 163  
 Neufeld, D. A., Wolfire, M. G., & Schilke, P. 2005, *ApJ*, 628, 260  
 Öberg, K. I., Boogert, A. C. A., Pontoppidan, K. M., et al. 2011, *ApJ*, 740, 109  
 Owen, E. R., Wu, K., Inoue, Y., Yang, H. Y. K., & Mitchell, A. M. W. 2023, *Galaxies*, 11, 86  
 Padovani, M. 2023, in *Physics and Chemistry of Star Formation: The Dynamical ISM Across Time and Spatial Scales*, 237  
 Padovani, M., Bialy, S., Galli, D., et al. 2022, *A&A*, 658, A189  
 Padovani, M. & Gaches, B. 2024, in *Astrochemical Modeling: Practical Aspects of Microphysics in Numerical Simulations*. Edited by Stefano Bovino and Tommaso Grassi, 189–231

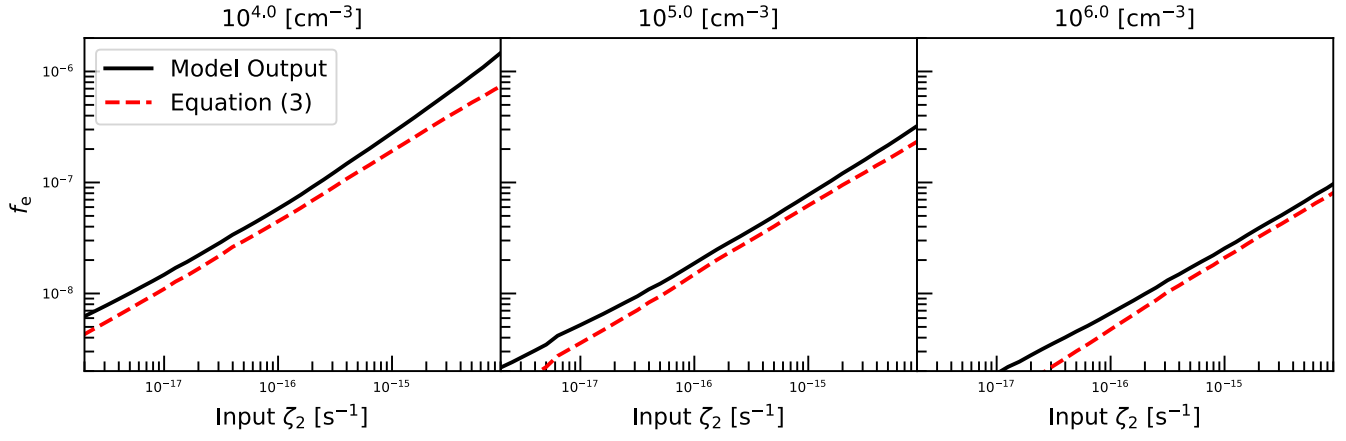
- Padovani, M., Galli, D., Hennebelle, P., Commerçon, B., & Joos, M. 2014, *A&A*, 571, A33
- Padovani, M., Galli, D., Scarlett, L. H., et al. 2024, *A&A*, 682, A131
- Padovani, M., Hennebelle, P., Marcowith, A., & Ferrière, K. 2015, *A&A*, 582, L13
- Padovani, M., Ivlev, A. V., Galli, D., et al. 2020, *Space Sci. Rev.*, 216, 29
- Padovani, M., Marcowith, A., Galli, D., Hunt, L. K., & Fontani, F. 2021, *A&A*, 649, A149
- Padovani, M., Marcowith, A., Hennebelle, P., & Ferrière, K. 2016, *A&A*, 590, A8
- Padovani, M., Marcowith, A., Sánchez-Monge, Á., Meng, F., & Schilke, P. 2019, *A&A*, 630, A72
- Peron, G., Casanova, S., Gabici, S., Baghmany, V., & Aharonian, F. 2024, *Nature Astronomy*, 8, 530
- Pineda, J. L., Goldsmith, P. F., Chapman, N., et al. 2010, *ApJ*, 721, 686
- Podio, L., Lefloch, B., Ceccarelli, C., Codella, C., & Bachiller, R. 2014, *A&A*, 565, A64
- Priestley, F. D., Viti, S., & Williams, D. A. 2018, *AJ*, 156, 51
- Purcell, C. R., Balasubramanyam, R., Burton, M. G., et al. 2006, *MNRAS*, 367, 553
- Purcell, C. R., Longmore, S. N., Burton, M. G., et al. 2009, *MNRAS*, 394, 323
- Qin, S.-L., Liu, T., Liu, X., et al. 2022, *MNRAS*, 511, 3463
- Redaelli, E., Bovino, S., Lupi, A., et al. 2024, arXiv e-prints, arXiv:2402.10852
- Redaelli, E., Sipilä, O., Padovani, M., et al. 2021, *A&A*, 656, A109
- Rosolowsky, E., Hughes, A., Leroy, A. K., et al. 2021, *MNRAS*, 502, 1218
- Sabatini, G., Bovino, S., & Redaelli, E. 2023, *ApJ*, 947, L18
- Schöier, F. L., van der Tak, F. F. S., van Dishoeck, E. F., & Black, J. H. 2005, *A&A*, 432, 369
- Shimajiri, Y., Takahashi, S., Takakuwa, S., Saito, M., & Kawabe, R. 2008, *ApJ*, 683, 255
- Shingledecker, C. N., Bergner, J. B., Le Gal, R., et al. 2016, *ApJ*, 830, 151
- Sofia, U. J., Cardelli, J. A., Guerin, K. P., & Meyer, D. M. 1997, *ApJ*, 482, L105
- Su, Y., Yang, J., Zhang, S., et al. 2019, *ApJS*, 240, 9
- Tibaldo, L., Gaggero, D., & Martin, P. 2021, *Universe*, 7, 141
- van der Tak, F. F. S., Black, J. H., Schöier, F. L., Jansen, D. J., & van Dishoeck, E. F. 2007, *A&A*, 468, 627
- van Dishoeck, E. F. 2014, *Faraday Discussions*, 168, 9
- Vink, J. 2022, arXiv e-prints, arXiv:2212.10677
- Viti, S., Collings, M. P., Dever, J. W., McCoustra, M. R. S., & Williams, D. A. 2004, *MNRAS*, 354, 1141
- Wakelam, V. & Herbst, E. 2008, *ApJ*, 680, 371
- Wakelam, V., Ruaud, M., Gratier, P., & Bonnell, I. A. 2019, *MNRAS*, 486, 4198
- Wolfire, M. G., Hollenbach, D., & McKee, C. F. 2010, *ApJ*, 716, 1191
- Womack, M., Ziurys, L. M., & Wyckoff, S. 1992, *ApJ*, 393, 188
- Yan, D.-H., Zhou, J.-N., & Zhang, P.-F. 2022, *Research in Astronomy and Astrophysics*, 22, 025016
- Yang, R.-z., de Oña Wilhelmi, E., & Aharonian, F. 2018, *A&A*, 611, A77
- Yang, R.-Z. & Wang, Y. 2020, *A&A*, 640, A60
- Yusef-Zadeh, F., Wardle, M., Rho, J., & Sakano, M. 2003, *ApJ*, 585, 319
- Zinnecker, H. & Yorke, H. W. 2007, *ARA&A*, 45, 481

## Appendix A: Comparison of electron fraction from our assumption and model prediction

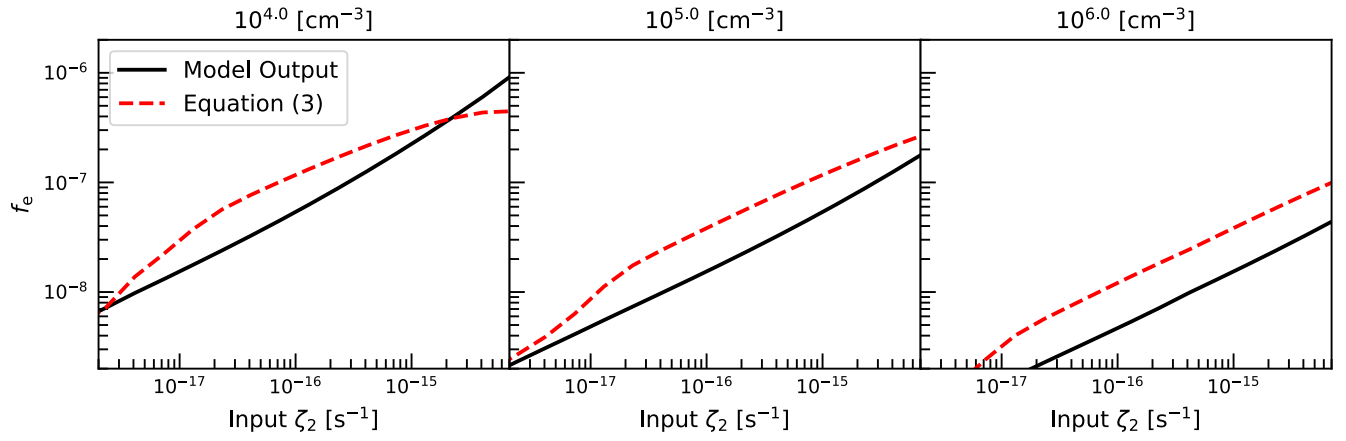
Figure A.1 shows the comparison between the electron fraction ( $f(e^-)$ ) obtained from model simulations and that of Eq. 3. As can be seen, our assumption in Eq. 3 gives reasonable results for both 3D-PDR and UCLCHEM simulations. The deviation between Eq. 3 and model prediction is within a factor of  $\sim 2$  for all 3D-PDR simulations and isothermal simulations from UCLCHEM. For the HMC simulations from UCLCHEM, the deviation is within a factor of 4 if  $10^{-17} \leq \zeta_2/s^{-1} \leq 10^{-14}$ . For  $\zeta_2 < 10^{-17} \text{ s}^{-1}$ , Eq. 3 underestimate the electron fraction since we did not consider the contribution of other ions (e.g.,  $C^+$ ,  $Mg^+$ ).

## Appendix B: The reaction rates that appears in the analytic approach

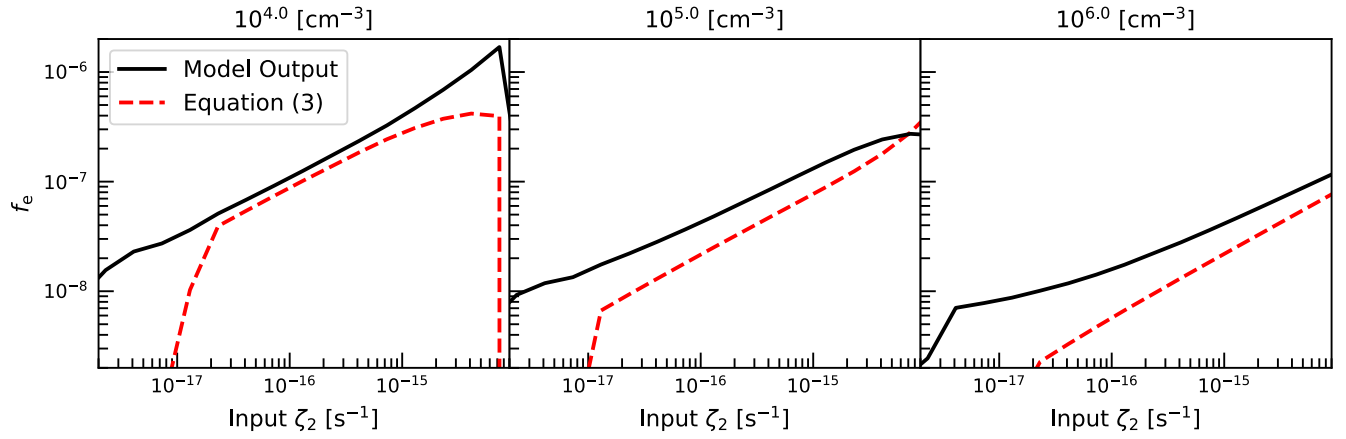
Table B.1 lists the reaction rates that appear in Sect.2, where the rates are taken from UMIST database (Millar et al. 2024).



(a) 3D-PDR



(b) UCLCHEM (isothermal)



(c) UCLCHEM (HMC)

**Fig. A.1.** (a): The electron fraction as a function of  $\zeta_2$  as obtained from the 3D-PDR output (black solid curves) and from Eq. 3 (red dashed curves). (b): The same as (a) while for the isothermal simulations from UCLCHEM. (c): The same as (a) while for the HMC simulations from UCLCHEM.

**Table B.1.** The reaction rates of reactions in Sect. 2.

Reactions	Rates $\text{cm}^{-3} \text{s}^{-1}$	Reactions	Rates $\text{cm}^{-3} \text{s}^{-1}$
$\text{H}_2 + \text{CR} \longrightarrow \text{H}_2^+ + \text{e}^-$	$0.88\zeta_2$	$\text{H}_2^+ + \text{H}_2 \longrightarrow \text{H}_3^+ + \text{H}$	$2.08 \times 10^{-9}$
$\text{H}_3^+ + \text{CO} \longrightarrow \text{HCO}^+ + \text{H}_2$	$1.36 \times 10^{-9} \left(\frac{T}{300}\right)^{-0.14} e^{\frac{3.4}{T}}$	$\text{H}_3^+ + \text{CO} \longrightarrow \text{HOC}^+ + \text{H}_2$	$8.49 \times 10^{-10} \left(\frac{T}{300}\right)^{0.07} e^{\frac{-5.2}{T}}$
$\text{H}_3^+ + \text{N}_2 \longrightarrow \text{N}_2\text{H}^+ + \text{H}_2$	$1.8 \times 10^{-9}$	$\text{H}_3^+ + \text{O} \longrightarrow \text{OH}^+ + \text{H}_2$	$4.65 \times 10^{-10} \left(\frac{T}{300}\right)^{-0.14} e^{\frac{-0.67}{T}}$
$\text{H}_3^+ + \text{O} \longrightarrow \text{H}_2\text{O}^+ + \text{H}$	$2.08 \times 10^{-10} \left(\frac{T}{300}\right)^{-0.4} e^{\frac{-4.86}{T}}$	$\text{H}_3^+ + \text{e}^- \longrightarrow \text{H}_2 + \text{H}$	$2.34 \times 10^{-8} \left(\frac{T}{300}\right)^{-0.52}$
$\text{H}_3^+ + \text{e}^- \longrightarrow \text{H} + \text{H} + \text{H}$	$4.36 \times 10^{-8} \left(\frac{T}{300}\right)^{-0.52}$	$\text{HCO}^+ + \text{e}^- \longrightarrow \text{CO} + \text{H}$	$2.4 \times 10^{-7} \left(\frac{T}{300}\right)^{-0.69}$
$\text{N}_2\text{H}^+ + \text{CO} \longrightarrow \text{HCO}^+ + \text{N}_2$	$8.8 \times 10^{-10}$	$\text{N}_2\text{H}^+ + \text{e}^- \longrightarrow \text{H} + \text{N}_2$	$3.06 \times 10^{-7} \left(\frac{T}{300}\right)^{-0.06}$
$\text{N}_2\text{H}^+ + \text{O} \longrightarrow \text{OH}^+ + \text{N}_2$	$1.4 \times 10^{-10}$	$\text{OH}^+ + \text{H}_2 \longrightarrow \text{H}_2\text{O}^+ + \text{H}$	$1.27 \times 10^{-9} \left(\frac{T}{300}\right)^{0.18}$
$\text{H}_2\text{O}^+ + \text{H}_2 \longrightarrow \text{H}_3\text{O}^+ + \text{H}$	$9.7 \times 10^{-10}$	$\text{H}_3\text{O}^+ + \text{e}^- \longrightarrow \text{OH} + \text{H} + \text{H}$	$3.05 \times 10^{-7} \left(\frac{T}{300}\right)^{-0.5}$
$\text{H}_3\text{O}^+ + \text{e}^- \longrightarrow \text{OH} + \text{H}_2$	$5.37 \times 10^{-8} \left(\frac{T}{300}\right)^{-0.5}$	$\text{H}_3\text{O}^+ + \text{e}^- \longrightarrow \text{H}_2\text{O} + \text{H}$	$7.09 \times 10^{-8} \left(\frac{T}{300}\right)^{-0.5}$